THE JOURNAL OF PHYSICAL CHEMISTRY C

UNIVERSITY OF EXETER

Subscriber access provided by the University of Exeter

C: Surfaces, Interfaces, Porous Materials, and Catalysis

Efficient Photoelectrochemical Performance of Gamma Irradiated g-C3N4 and its g-C3N4@BiVO4 Heterojunction for Solar Water Splitting

Nurul Aida Mohamed, Habib Ullah, Javad Safaei, Aznan Fazli Ismail, Mohamad Firdaus Mohamad Noh, Mohd Fairuz Soh, Mohd Adib Ibrahim, Norasikin Ahmad Ludin, and Mohd Asri Mat Teridi

J. Phys. Chem. C, **Just Accepted Manuscript** • DOI: 10.1021/acs.jpcc.9b00217 • Publication Date (Web): 06 Mar 2019

Efficient Photoelectrochemical Performance of Gamma Irradiated g-C_3N_4 and its g-C_3N_4@$BiVO_4$ Heterojunction for Solar Water Splitting

Nurul Aida Mohamed[†], Habib Ullah[‡] , Javad Safaei[†], Aznan Fazli Ismail[§,□], Mohamad Firdaus Mohamad Noh[†], Mohd Fairuz Soh[†], Mohd Adib Ibrahim[†], Norasikin Ahmad Ludin[†] and Mohd Asri Mat Teridi[†]

[†]Solar Energy Research Institute (SERI), Universiti Kebangsaan Malaysia, 43600 UKM Bangi, Selangor, Malaysia

[‡]Renewable Energy Group, College of Engineering, Mathematics and Physical Sciences, University of Exeter, Penryn Campus, Cornwall, TR10 9FE, United Kingdom.

[§]Nuclear Science Program, Faculty of Science and Technology, Universiti Kebangsaan Malaysia, 43600 UKM Bangi, Selangor, Malaysia

[□]Centre for Frontier Science, Faculty of Science and Technology, Universiti Kebangsaan Malaysia, 43600 UKM Bangi, Selangor, Malaysia

Abstract

Comprehensive experimental and density functional theory simulations have been performed for the enhanced photoelectrochemical performance of gamma irradiated g-C_3N_4 and its heterojunction with $BiVO_4$. The structure and morphology of g-C_3N_4@$BiVO_4$ as a heterojunction were analyzed and verified from the correlation of experimental and theoretical data. It is found that gamma radiations have changed the bonding structure of

g-C_3N_4 which ultimately reduces the optical bandgap energy. Moreover, the performance of gamma-irradiated g-C_3N_4 is two-fold, compared to that of non-irradiated one; increases from 3.59 to 5.86 μAcm^{-2} at 1.23 V versus Ag/AgCl in 0.5 M Na_2SO_4 electrolyte solution (pH 7). Finally, it is observed that the performance of gamma irradiated g-C_3N_4 in g-C_3N_4@$BiVO_4$ heterojunction increased from 0.53 mA cm^{-2} to 1.38 mA cm^{-2}, compared to that of the non–irradiated one. In summary, it has been concluded that gamma-irradiated g-C_3N_4 and its heterojunction is potentially be applied in PEC solar water splitting.

1. Introduction

Practical solar water splitting requires light absorption, separation and collection of photogenerated charge carriers, and charge-carrier transport to catalytic sites to produces gases which must be safely and economically separated and stored[1]. Photoelectrolysis of water produces molecular hydrogen and oxygen which is an obvious and direct way to store solar energy as fuel [2–4]. Hydrogen stored its energy in the form of a chemical bond which directly or indirectly reacts with oxygen to release energy. The efficient and cost-effective solar water splitting into H_2 and O_2 to produce solar fuel, a renewable energy carrier, has become a hot research area since 1970s. This research was spurred by the oil crisis of that period, when the famous paper of Fujishima and Honda [5] showed H_2O splitting into H_2 and O_2. This solar water splitting experiment was achieved by near UV light with the help of photoelectrochemical (PEC) cell.

Over the last decade, significant research efforts have been carried out on the efficient hydrogen production. Numerous semi-conducting materials are employed for the optimum hydrogen production such as transition metal oxides, perovskites, tuning their properties via doping, making heterojunctions, and tandem cells. All these

materials/techniques were chosen based on their flexibility, cost effectiveness, and ease of availability. As per our literature review is concerned, the effect of gamma radiation onto the g-C_3N_4 has become a novel approach in this research area, which is yet be explored.

Exposure of material to ionizing radiation (e.g. X-rays, gamma, beta, alpha and neutron) may change the physical and chemical properties due to the bond disruption which in turn affects the optical, electrical and structural of the material [6]. The innovation by employing the gamma irradiation on g-C_3N_4 semiconductor was chosen due to its high penetration power compared to other ionizing radiation, not contaminate as well as not induce the material to become radioactive. In addition to that, the alteration to the chemical bonds due to the irradiation may improve the materials performance [7]. A few research has

reported the positive effect of gamma radiation of materials. The effect of gamma radiation on the thin film performance of TeO_2 [8] was reported to linearly improve the current with the increase of gamma dose up to 7 Gy before decreases as gamma dose approached to 13 Gy. In addition to that, the effects of gamma radiation on the absorption spectra and optical energy gap of SeO_2 thin film [9] was reported to significantly increases the optical absorption due to changes on the chemical structure of the absorbing species. Furthermore, gamma radiations have been developed for the preparation of metal nanoparticles i.e., Ag [10] ,Ni [11], and Zn [12]. The effect of gamma radiation on the formation, structural, and optical properties of CdS [13], PbS [14], $Fe_{3-x}O_4$ [14], and ZnO [15] thin films were also reported to improve the bandgap from 3.25 to 3.20 eV, even though deteriorate the absorption coefficient from 0.62 to 0.73 eV. Therefore, this research aims to investigate the effect of gamma irradiation on g-C_3N_4 and g-C_3N_4/$BiVO_4$ in photoelectrochemical (PEC) solar water splitting application.

The g-C_3N_4 can be synthesized through nitrogen-rich precursors such as cyanamide, dicyandiamide, melamine, thiourea, and urea. In this work, urea was chosen as a

potential precursor due to its availability and low material synthesis cost. Urea was reported as an excellent precursor for the synthesis of sheet-like g-C_3N_4 with high specific surface area and high porosity [16–23]. However, under visible light radiation, the g-C_3N_4 exhibit weak photocatalytic activity due to its moderate bandgap (2.7 eV) [24]. Gamma irradiation was employed on g-C_3N_4 to improve the PEC performance whereas the $BiVO_4$ as heterojunction was preferred as a potential material to reinforce its performance in water splitting application. The formation of the heterojunction is a useful to enhance the PEC properties, meanwhile matching the band potentials is expected to improve the photo-conversion efficiency of photogenerated charge carriers. The $BiVO_4$ is a n-type semiconductor and has been considered as a promising photoanode [25–27] due to its narrow bandgap (2.4 eV), more active in visible light [28] , and can achieve about 9% of solar-to-chemical conversion. The $BiVO_4$ has special valence-band position to protoxidize H_2O, while its conduction band is located close to the H_2 evolution potential [29]. The other advantages of $BiVO_4$ are non-toxicity, low cost, and environmental friendly material.

Herein, the g-C_3N_4 was irradiated with gamma radiation before deposited onto a substrate through a spin coating method. Then, in a separate experiment, $BiVO_4$ was deposited as

heterojunction through electrodeposition method. To better utilize solar radiation for the improved photocatalytic activity, these two strategies, gamma radiation and heterojunction were employed. Finally, the density functional theory (DFT) simulations was performed to verify the experimental data. The calculated formation energy concludes the stability of g-C_3N_4@$BiVO_4$ interface (heterojunction) and consequences van der Waal type interaction.

2. Experimental

2.1. Materials

Urea (CH_4N_2O, ACS reagent 99.0%-100.5%), methanol (CH_3OH), R&M chemical, Bismuth (III) nitrate ($Bi(NO_3)_3 \cdot 5H_2O$, ≥98.0%) and vanadium (IV) oxide sulfate ($VOSO_4 \cdot xH_2O$, 97%) were purchased from Sigma Aldrich. Nitric acid (HNO_3, 69%), potassium hydroxide (KOH, pellets) and sodium sulphate (Na_2SO_4, >98.0%) were obtained from R&M chemicals meanwhile sodium acetate (CH_3COONa, >99.0%) from ACSq. All solutions were prepared using high thermal water purification system (Termo scientific smart2pure 6UV/UF).

2.2. Preparation and Synthesis of g-C_3N_4

Fluorine-doped tin oxide glass slides (FTO, TEC 8, ~ 8Ω sq^{-1} Pilkington) were prepared with a 1.0×2.0 cm^2 area. The FTO glass was cleaned with acetone, ethanol, and deionized water for 15 minutes successively in an ultrasonic bath and then dried in air. A total 3g of Urea was poured into 50 ml alumina crucible in order to prepare the g-C_3N_4 through a spin coating technique followed by thermal polymerization at the temperature of 520 °C for 30 minutes [30]. This temperature is essential to thermodynamically driven the reaction which forms g-C_3N_4 from urea, removing oxygen molecules. Finally, a milky yellow powder is formed. A total of 30~40 mg/mL of the powder was dispersed in deionised water and washed for three times to remove any extra organic compound followed by drying in an oven at the temperature of 40 ˚C for 24 hours. Then, the g-C_3N_4 powder was dispersed in methanol at the ratio of 0.5 mg/L prior irradiated with gamma radiation at the dose of 2, 4, 6, 8 and 10 Gy using a Gamma Cell (model 220 Excel) with Cobalt-60 radioactive source.

For deposition of one-layer g-C_3N_4 thin film, 10 µL of the suspension was spun on a precleaned FTO at 2500 rpm with the acceleration of 500 rpm/s for 10 s. The thin film was dried for 15 minutes at a temperature of 70 °C to remove alcoholic molecules followed by the annealing at a temperature of 350 °C for 30 minutes.

2.3. Synthesis of $BiVO_4$

The electrodes of $BiVO_4$ were prepared by an electrodeposition procedure [27] .For the electrodeposition, solutions were prepared by dissolving 10 mM $Bi(NO_3)_3$ in a solution of 35 mM $VOSO_4$ at < pH 0.5 with HNO_3. Then, 2 M sodium acetate act as a stabilizer was employed to stabilize the solution from the (pH~5.1) to (pH~4.7) with a few amounts of concentrated nitric acid. The optimum for the electrodeposition $BiVO_4$ occur at pH 4.7, where the solution contains Bi (III) and V (IV) ions. Beyond the pH 5.1 value, the solution becomes precipitate, however, at lower pH (<pH 2), the Bi (III) and V (IV) ions no deposited on the substrate as reported by Seabold and Choi, 2012. [31]

A standard three-electrode cell was employed for the electrodeposition, where FTO is used as working electrode, Ag/AgCl (3 M KCl) as reference, and platinum as counter

electrode. A potentiostat/galvanostat modulab solatron analytical was used for electrodeposition and all subsequent electrochemical studies. Deposition of amorphous Bi−V−O films was carried out potentiostatically at 1.9 V vs Ag/AgCl for 5 min at 70 °C (ca. 2 mA/cm^2). All thin films were rinsed and then annealed at 500 °C for 1 h in air, with 2 °C per minute ramping rate. The pure $BiVO_4$ was obtained by dissolving the V_2O_5 in 1 M KOH at 20 min stirring. Finally, yellow color was formed on the thin film.

2.4. Characterization methods

The electrochemical properties of the samples were examined with the help of Autolab potentiostat/galvanostat PGSTAT 204 at room temperature, using three electrode configurations with Ag/AgCl (3M NaCl) as reference electrode and 0.5 M Na_2SO_4 (pH 7) as electrolyte. Platinum was used as counter electrode in a quartz container. The Xenon lamp with 100 mW/cm^2 intensity was used as solar light simulator. The electrochemical circle fitting of Nyquist plots was analysed using Nova Software. The electrochemical measurements were conducted in dark where incident light intensity of 100Mw cm^{-2}, potential range from -1 to 1.23 V, and scan rate of 20 mVs^{-1} is employed. PEC

measurements were performed on 1.0 cm^2 area of the working electrode. UV-vis absorption spectrophotometer Perkin Elmer Lambda 950 was used for the characterization of optical properties. The physical and morphological properties of the samples were characterized by X-ray Diffraction (XRD), Fourier Transform Infra-Red-Near Infra-Red (FTIR-NIR) with imaging system (Perkin Elmer Spectrum 400 FT-IR/FT-NIR & Spotlight 400 Imaging System), Field Emission Scanning Electron Microscopy (FESEM-EDX) (Supra VP 55) and Atomic Force Microscopy (AFM) (NanosurfeasyScan 2). The X-ray Photoelectron Spectroscopy (XPS) is performed to analyse the chemical bonding, band structure, and elemental composition of the photoelectrodes, using Al Ka x-ray gun.

2.5. First principles study

First principles DFT calculations were performed on Quantum-ATK [32] while the results are visualized on VESTA and Virtual NanoLab Version 2017.1 [33]. $BiVO_4$ with Hall symmetry space group of I2/b [34] is used as such. After optimizing the lattice parameters of the bulk unit cell; a supercell (2x2x2) was constructed, from which $BiVO_4$(001) slab was

built. Thickness of the slab was kept as four primitive unit cells of $BiVO_4$ (10 Å thickness having 96 atoms), to ensure that the centre of the slab can be regarded as the bulk phase. As discussed in our previous work, the (001) termination possesses low surface energy and as a result represents the most probable surface termination [35]. Stability of these different slabs are confirmed from their positive surface formation energy and electrostatic potential. Single layer g-C_3N_4 is considered for simulations, the structure of single layer g-C_3N_4 is illustrated (*vide infra*). Generalized gradient approximation (GGA) with the Perdew-Burke-Ernzerhof (PBE) exchange-correlation functional and double Zeta Polarized (DZP) basis set is used for the structural and energy optimization due to its superiority over hybrid pseudopotentials [36] .Moreover, linear combination of atomic orbitals (LCAO) method is used for Bi, V, Ti, C, N, H, and O atoms [37]. A 7x7x3 Monkhorst-Pack k-grid and energy cutoff of 1200 eV is used for the $BiVO_4$ unit cell while a 5x5x1 k-point mesh is used for its slabs. 7x7x7 Monkhorst-Pack k-grid and energy cutoff of 900 eV is used for monolayer g-C_3N_4, and 5x5x1 k-point mesh with 1200 eV cutoff energy for g-C_3N_4@$BiVO_4$(001) heterostructure. The band structure calculations were performed with TB09LDA functional of meta-GGA, which can accurately reproduce the experimental

bandgaps. Recently, Tran and Blaha reported that this accuracy is due to local density ρ(r) (as in LDA), the gradient of density ∇ρ(r) (as in GGA), and the kinetic-energy density τ(r) [38]. The parameter c-equations of the Tran and Blaha XC functions have been installed to reproduce the experimental bandgap excellently [38]. Density of states (DOS), partial density of states (PDOS), band structure and effective masses of photogenerated electrons and holes are also calculated. The DFT occupied and unoccupied DOS are considered as the VB and CB edges, respectively; separated by an energy equal to the known optical bandgap [39].

3. RESULTS AND DISCUSSION

3.1. Structural analysis

XRD plots of FTO, g-C_3N_4 and gamma radiated g-C_3N_4 along with their corresponding $BiVO_4$ heterojunctions are illustrated in Fig. 1. XRD peaks of g-C_3N_4 are in good agreement with the hexagonal carbon nitride structure with the lattice constants a= 0.4742 nm and c= 6.7205 nm, which is in according with the literature values of JCPDS 87-1526. The strong XRD peak at 2θ = 27.4° is originated from the (002) interlayer diffraction of

graphitic-like structures, corresponding to an interlayer distance of d= 0.326 nm [40–42]. Besides g-C_3N_4, 2θ = 13.3° (d=0.663), low angle diffraction peak derived from in-planar repeated triazine unit. In case of g-C_3N_4 powder, two peaks ca. at (100) and (002) planes were observed which correspond to interplanar separation of g-C_3N_4 sheets and interlayer stacking of the aromatic systems, respectively [27,42].

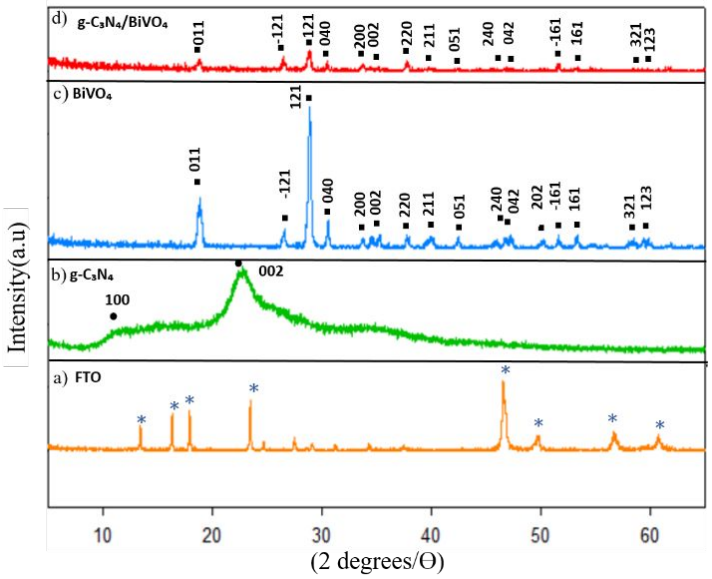

Fig. 1 XRD peaks of (a) FTO (b) g-C_3N_4 (c) $BiVO_4$ and (d) gamma radiated g-C_3N_4@$BiVO_4$.

Thin films of $BiVO_4$ were successfully deposited through a single step, using electrodeposition method. In case of XRD analysis (Fig. 1c), the characteristic diffraction

peaks are observed at 2θ = 18.99°, 28.82°, 28.96°, 30.54°, 34.50°, 35.22°, 37.87°, 39.78°, 42.48°, 46.73°, 47.29°, 50.31°, 53.22°, 58.53° and 59.49°. These peaks coincided very well with the monoclinic clinobisvanite structure of $BiVO_4$ (JCPD file no. 00-014-0688). The monoclinic clinobisvanite is more prevalent under normal condition and highly photocatalytically active as well [25–27,43]. Due to nearly amorphous structure of g-C_3N_4, the peak from g-C_3N_4 is not clearly visible for gamma radiation in g-C_3N_4@$BiVO_4$ (Fig. 1d). Results and analysis of these finding led us to conclude that there are no impurity diffraction peaks in the XRD patterns of g-C_3N_4@$BiVO_4$, can be indexed as hexagonal (JCPDS file no. 01-087-1526) for g-C_3N_4, monoclinic (JCPDS file no. 01-074-4894) for $BiVO_4$. The peak intensity of (121), (040), (051), (042) and (161) support that g-C_3N_4@$BiVO_4$ has better crystallized structures [44,45]. It can be concluded that gamma radiation has negligible effect on the crystalline structure of g-C_3N_4@$BiVO_4$ which is due to the close packing of atoms.

3.2. Chemical composition

FT-IR has been used to identify organic, polymeric, and inorganic materials in the resulted samples. FT-IR spectra of the g-C_3N_4 and gamma irradiated Gy (2,4,6,8,10) g-C_3N_4 are

shown in Fig. 2. Five peaks can be clearly observed in the FT-IR spectra where the strong peak at ca. 810 cm^{-1} corresponds to the out of plane ring bending of the triazine unit [40,46]. The peak ca. at 1630 cm^{-1} corresponds to the C-N heterocycle, stretching vibrations modes, whereas the peaks ca. at 1450 and 1250 cm^{-1} can be assigned to aromatic C-N stretching vibration modes [47,48]. The broad bands between 3000 cm^{-1} and 3600 cm^{-1} are attributed to the secondary and primary amines, respectively [40,49]. Gamma radiation modify and change the chemical structures of pure g-C_3N_4 for the peak ca. at 810 cm^{-1}, denotes triazine unit and became sharper at 8Gy g-C_3N_4. Meanwhile, 1250 cm^{-1} peak represent the aromatic C-N and became strong light absorber due to ionizing of gamma radiation. The sharp peak ca. at 1250 cm^{-1} is an indication of good crystallinity of g-C_3N_4 due to gamma radiation [46]. Obviously, the characteristic peaks of 3200 cm^{-1} became stretching upon gamma irradiation. According to knoll [50], when radiation interacts with semiconductor, the energy deposition always leads to the creation of equal number of holes and electrons on material. Thus, the energy from gamma radiation may interrupt the C-N bonding and electrons become stronger and easily migrate in atom.

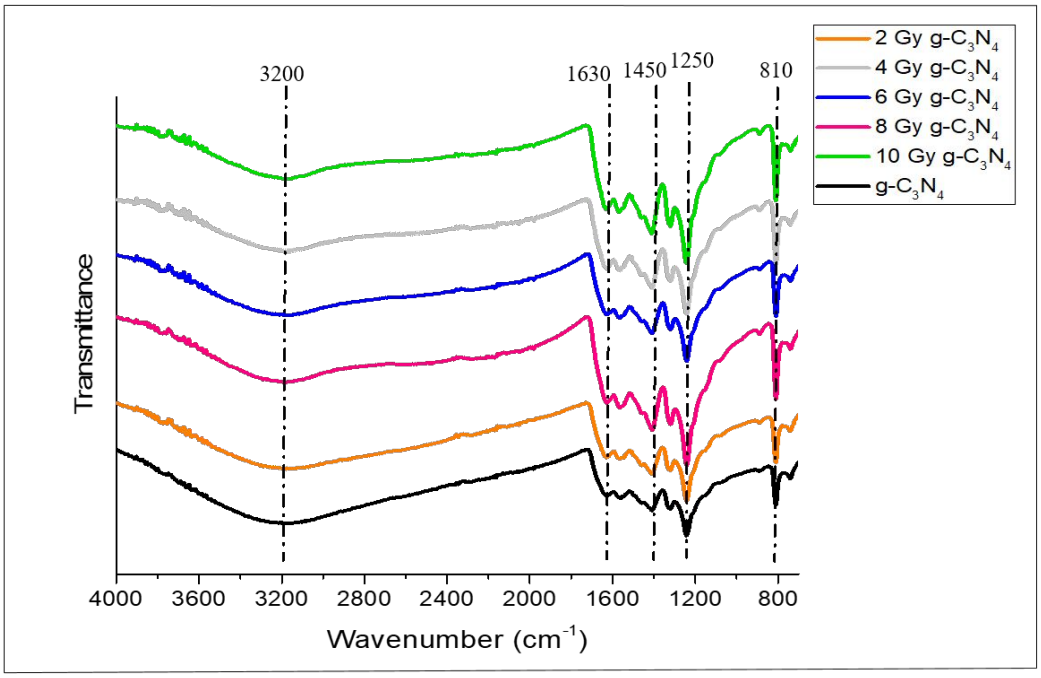

Fig. 2 FT-IR spectra of g-C_3N_4 and irradiated g-C_3N_4.

3.3. Electronic interaction analysis

XPS analysis was carried out to get additional insight into the chemical composition of g-C_3N_4 and radiated-g-C_3N_4 on thin films, as shown in Fig. 3. High resolution spectra of C 1s ca. at 284.60 and 288.0 eV are shown in Fig. 3a. The peak for 284.6 eV can be attributed to the adventitious carbon, adsorbed on the surface and the peak of 288.0 eV is related to sp^2 hybridizes carbon in N containing aromatic rings (N-C=N) of g-C_3N_4 [51]. The high resolution XPS scan of N1s for g-C_3N_4 and radiated g-C_3N_4 are given in Fig. 3b. There are four main peaks ca. at 398.4, 399.4, 400.7, and 403.5 eV. The main peaks ca.

at 398.4 and 399.4 eV are assigned to the sp^2 hybridized aromatic of N to carbon atoms in triazine unit (C-N=C) and the tertiary N bonded to carbon atoms ($N-(C)_3$), respectively. The peak ca. at 400.7 eV belongs to the amino group (C-N-H), from the defect of g-C_3N_4 [27,42,52]. Additionally, the peak for 403.5 eV shows π-excitation, which comes from charging effect or positive charge localization in the heterocycles [51,53]. Both XPS spectra of C1s and N1s reveal that an electronic interaction occurs due to gamma radiation on g-C_3N_4, indicating that gamma radiation has produced a nice contact interfaces in the samples.

When photon interacts, it might be absorbed and disappear or it might be scattered, changing its direction of travel, with or without loss of energy [54]. The gamma radiation causes the bonding between carbon and nitrogen to break and modified the structure (see Fig. 3). This is due the ionization between the metallic bond. Ionization will enhance the kinetic energy of the electrons or excites the electrons to a higher energy level. However, ionization can also make a displacement in the material [55]. This is clearly seen in XPS images as the amplitude intensity of XPS for radiated g-C_3N_4 is less than that of pure g-C_3N_4. The breaking of carbon and nitrogen bond induces the formation of free-

carriers such as carbon and nitrogen. The free carriers then react with intrinsic oxygen in carbon nitride structure to form extra oxygen bonding that is clearly illustrated in the FTIR spectra (see Fig. 2). The reason behind this is, the free carbon atoms are more willing to make bonding with more electronegative oxygen compared to that of less electronegative nitrogen.

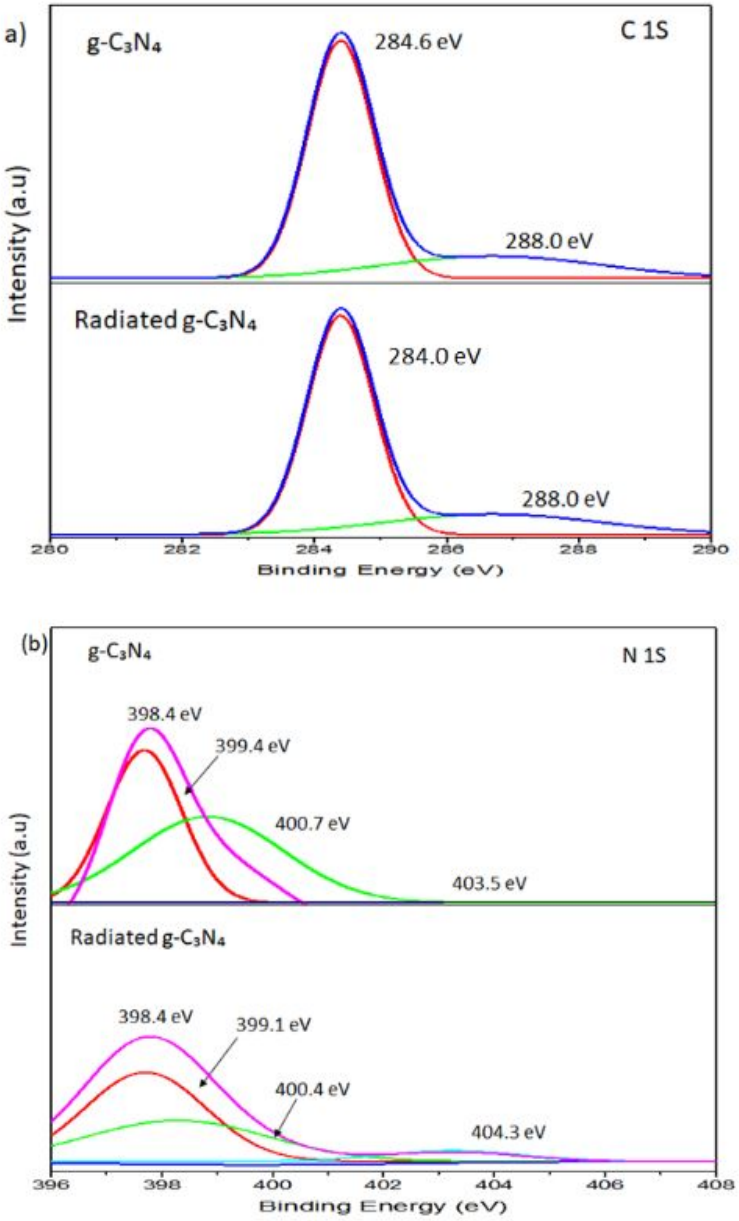

Fig. 3 XPS survey scans of a) C 1s and b) N 1s for g-C_3N_4 and radiated g-C_3N_4.

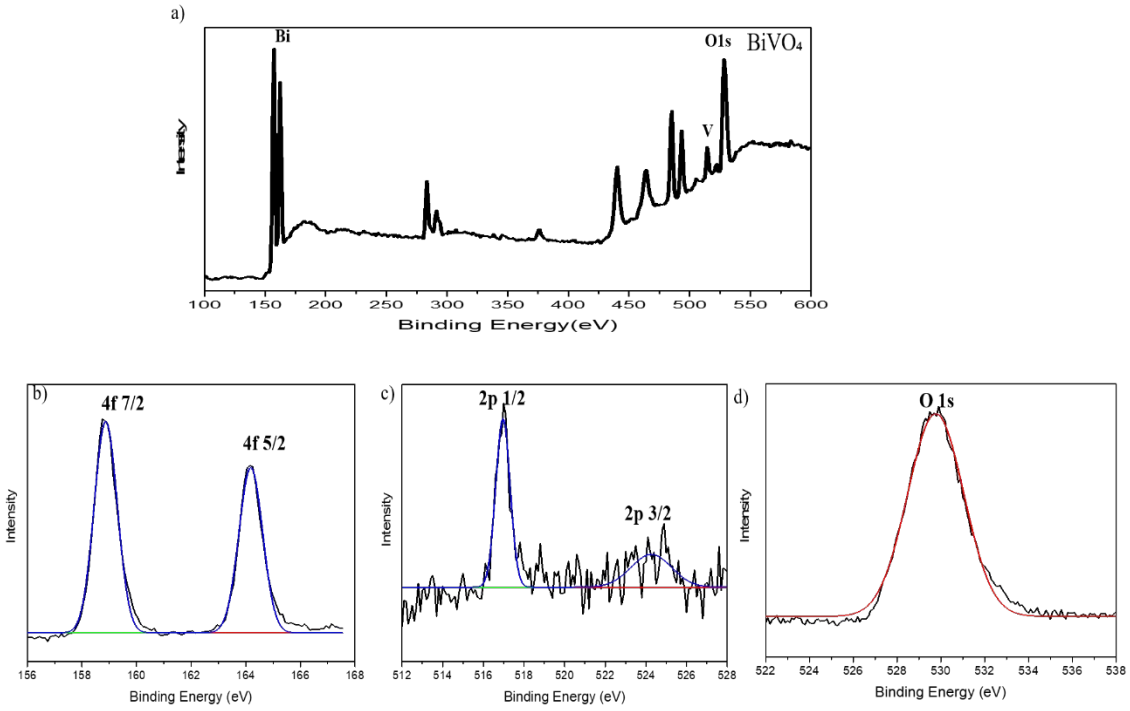

Fig. 4 X-ray photolectron spectra (XPS) survey spectrum for $BiVO_4$. High resolution X-ray photoelectron spectra of as deposited Bi-V-O film showing the b) Bi 4f, c) V 2p and d) O1s.

In (Fig. 4), the full survey spectra of $BiVO_4$ and their elements such as Bi, V, O are displayed from the XPS spectrum. It is clearly seen that g-C_3N_4/$BIVO_4$ thin film, does not influences the peak intensity for C1s and N1s due to the overlap of g-C_3N_4 and $BiVO_4$. The thickness of $BiVO_4$ around 365 nm will cover all the g-C_3N_4 surface and consequences, overlapping with elements of Bi, V and O. The high resolution XPS

spectra of deposited Bi-V-O film show the Bi 4f, V 2p peaks and O 1s. The position of the Bi and V peaks matches very well with those of Bi^{3+} and V^{5+} ions in oxides. The peaks of $BiVO_4$ are 4f 7/2 (159.0 eV), 4f 5/2 (164.45 eV), 2p ½ (516.30 eV), 2p 3/2 (525.0 eV) and O 1s (530. 49 eV) [27,31].

3.4 Optical properties and Band Gap Energy

The optical absorption spectrum is one of the most important tools for developing the energy band diagram. Fig. 5 shows an absorption spectrum for g-C_3N_4 and radiated g-C_3N_4 in liquid phase. The absorption spectrum of g-C_3N_4 and gamma radiated g-C_3N_4 in the wavelength range of 200 -700 nm are show in (Fig. 5a). The absorption of amino peak is located at 230 nm and the strong absorption band ca. at 320 nm shows carbon nitride bond in conjugation [56,57]. All these peaks indicate that g-C_3N_4 is sussesfully synthesized from urea. However, ionizing from gamma radiation modify and change the peak intensity of g-C_3N_4. Compared with pure g-C_3N_4 sample, radiated g-C_3N_4 samples show an intensive absorption ca. at 400 nm in the visible light region. This broad absorption ban

peak may arise due to the ionizing effect on bonding g-C_3N_4. Particularly, radiated g-C_3N_4, 8 Gy presents the most intensive broad absorption in the visible light region.

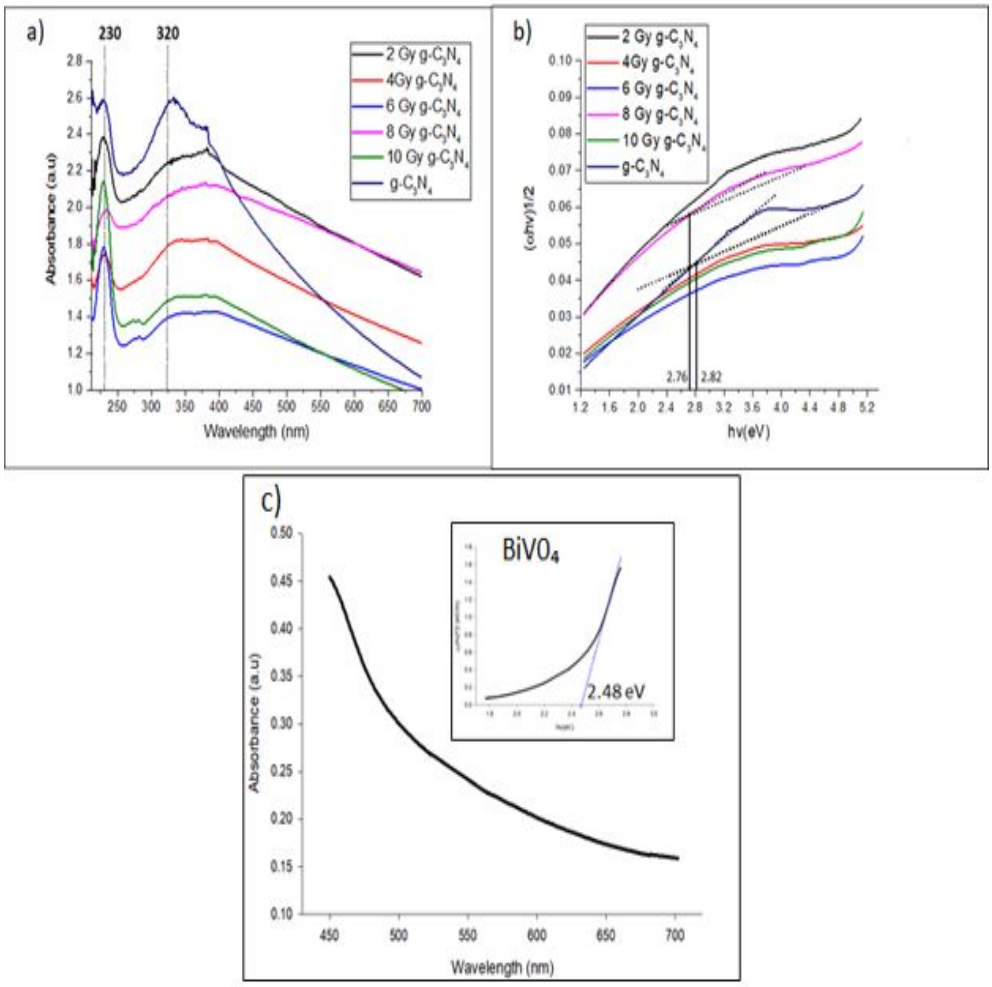

Fig. 5 a) UV-Vis absorbance spectra of g-C_3N_4 and radiated g-C_3N_4 b) estimation of bandgap energy by a Tauc Plot and c) $BiVO_4$ absorption UV-Vis (insert: estimation of band gap).

Obviously, the value of optical band gap decreases from 2.82 to 2.76 eV when g-C_3N_4 was treated by gamma radiation (see Fig. 5b). The reported band gap energies of g-C_3N_4 from urea in the range 2.69 to 2.88 eV depend on the different reaction parameter (annealing temperature, duration and atmosphere effect) [58] Dong et al.[48] reported 2.72 eV band gap for g-C_3N_4, synthesized from urea by the pyrolysis technique [48]. Meanwhile, Su et al [59] reported 2.58 eV (band gap) for g-C_3N_4, synthesized by hydrothermal process. Due to the ionizing from gamma radiation, the band gap for g-C_3N_4 decrease to 2.76 eV. Furthermore, Arshak and Kerostynska [60] reported the decrease in the optical band gap, from 3.75 eV for as deposited TeO_2 thin films to 3.45 eV for the gamma radiation on TeO_2 thin films for a dose of 36Gy. Ahmad et al. [61] also reported that gamma radiation shifted the Fermi level and the reduction in optical band gap from 2.14 to 2.06 eV, 2.19 to 1.99 eV and 2.25 to 2.09 eV of thin films of $Cd_5Se_{95-x}Zn_x$ (x = 0,2,4) after radiated on 75 kGy of gamma radiation. Meanwhile, Al-Hamdani et al. [15] found that, the gamma radiation also effect the performance of ZnO thin films and the band gap decrease from 3.25 to 3.2 eV. This decrease in optical band gap is basically due to the increase in the energy width of band tails of localized state, similar observations have been reported by other researcher

as well [29,62,63]. Meanwhile, (Fig. 5c) shows a photoanode absorption and the direct band gap transition of $BiVO_4$ thin films. The absorption was determined from the plots of $(\alpha hv)^2$ vs (hv) and the estimated bandgap energy is 2.48 eV [27,44,45].

3.5 Morphology

The surface morphology of g-C_3N_4, and radiated g-C_3N_4 along with their corresponding $BiVO_4$ heterojunctions are determined by FESEM-EDX and mapping with 200 nm resolutions. These films consisted of mesoporous g-C_3N_4 and look like a “seaweed” architecture picture structure as shown in (Fig. 6). Both FESEM images show that gamma radiation does not influence the morphology of the g-C_3N_4.

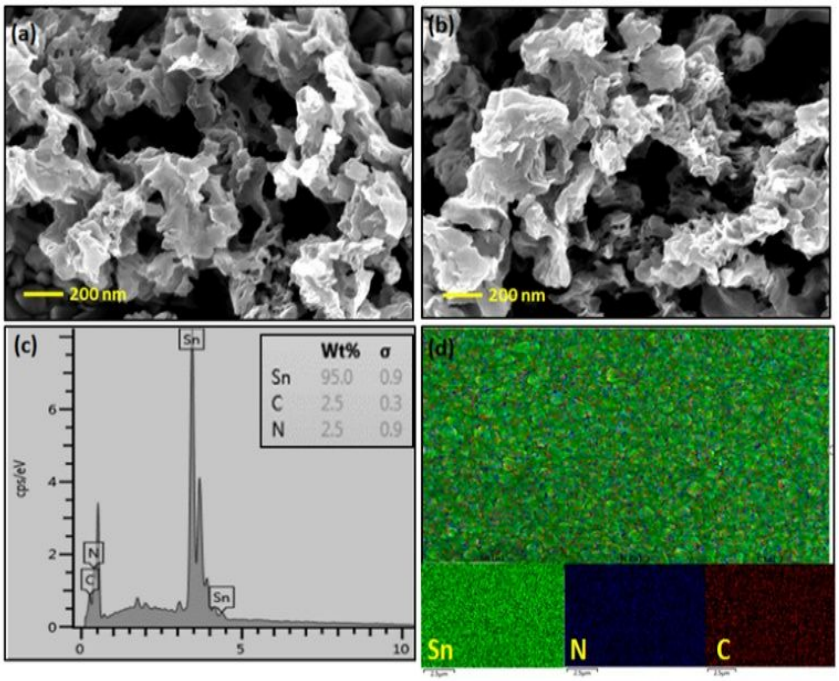

Fig. 6 FESEM-EDX images of (a) g-C_3N_4 (b) radiated g-C_3N_4 (8Gy), (c) (d) EDX and mapping of g-C_3N_4.

g-C_3N_4 is distributed on the surface of FTO by spin coating method. Several processing parameters are involved in the spinning process such as solution viscosity, solution concentration, spin time, and spin speed [64]. This technique is necessary which form a uniform layer to prevent a pinhole and large surface area for absorbing more light [44,65,66]. The existences of the elements of C and N in the samples was supported by EDX analysis as shown in (Fig. 6c). It can be observed no other impurity peak was detecting, except

the peak of Sn (probably was attributed to the FTO). The mapping results are supported in (Fig. 6d) to ensure that the g-C_3N_4 is uniformly distributed on thin films. The blue and red color are good indication for the elements of N and C, respectively.

Surface roughness of g-C_3N_4 and gamma radiated g-C_3N_4 were compared and presented in (Fig. 7(a-b) and table 1 along with their 3D view. Although, the AFM images show less noticeable changes in thin films topology whereas the gamma radiated g-C_3N_4 has recorded the highest surface roughness compared to pure g-C_3N_4. Hence, this indicate that gamma radiation on the g-C_3N_4 already transform the topology of the films. Generally, high surface roughness and small grain size can significantly affect the PEC performance, as more sites are exposed in the photocatalytic reaction [27,66,67].

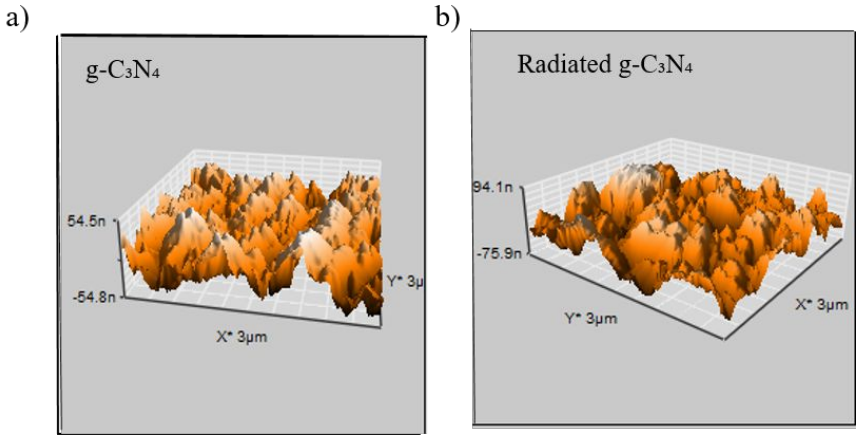

Fig. 7 AFM images for a) g-C_3N_4 and b) gamma radiated g-C_3N_4.

Table 1 Surface roughness of g-C_3N_4 and gamma radiated g-C_3N_4 determined by AFM.

Sample	Surface roughness (nm)
g-C_3N_4	19.72
Radiated g-C_3N_4	28.24

Under visible light irradiation, $BiVO_4$ has a direct bandgap of approximately 2.4 eV, allowing efficient absorption of photons. Therefore, the formation of a heterojunction of g-C_3N_4 with $BiVO_4$ is a good strategy to improve the photo-conversion efficiency of photogenerated charge carriers. The ability of $BiVO_4$ to absorb visible light would achieve about 9% of solar to chemical conversion. The development of heterojunction with $BiVO_4$ suppresses its charge recombination by improving the charge transport properties [27,52,66]. Furthermore, various deposition methods have been employed to synthesize $BiVO_4$ such as chemical bath deposition (CBD), Aerosol - assisted chemical vapor deposition (AACVD), electrodeposition and hydrothermal. Herein, the heterojunction is established

by electrodeposition method, an useful approaches to enhances the PEC properties. Electrodeposition has the distinctive advantages of being simple, low cost, and easy scalable while enabling deposition of the material of interest on the conductive substrate and not on the chamber wall.

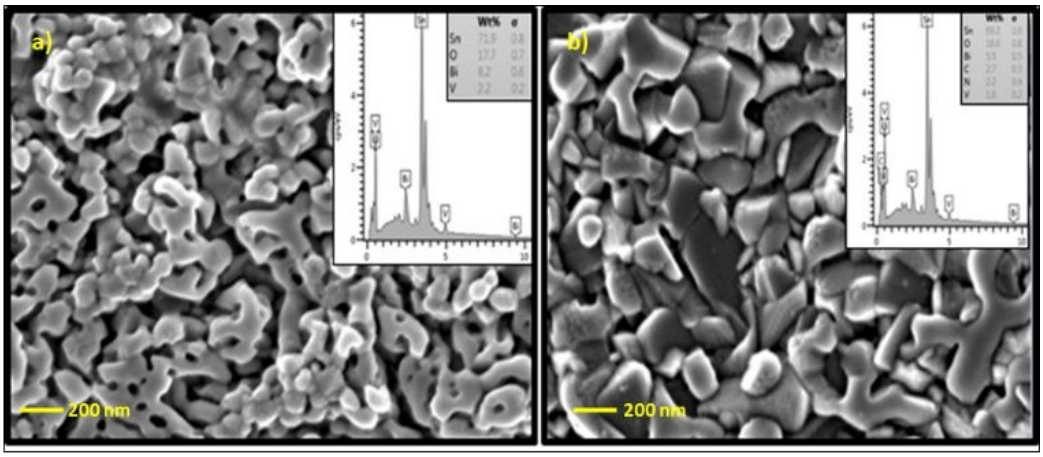

Fig. 8 FESEM-EDX of a) $BiVO_4$ and b) gamma radiation on g-C_3N_4@$BiVO_4$.

The FESEM-EDX surface morphology of the $BiVO_4$ and gamma radiated g-C_3N_4@$BiVO_4$ thin film are shown in (Fig. 8a) and b). It is clearly seen that the $BiVO_4$ morphology comprised of a “flower” like architecture image. Furthermore, for the gamma radiated g-C_3N_4@$BiVO_4$, some of the particles seemed to agglomerate and form high rough surface. This result is also in consistent with results obtained from AFM analysis, shown in (Fig.9). Interestingly, the agglomerated morphology of $BiVO_4$ would enlarge the active sites at the

interface between photoanode and the electrolyte, which will enhance the light absorption. Therefore, more electrons and holes would participate in the reaction at the interface which ultimately improve the photocatalytic activities. However, the images for unirradiated g-C_3N_4 with heterojunction $BiVO_4$ are not display as gamma radiation does not influence the structure of g-C_3N_4, see the discussion of (Fig.6). The existence of Bi, V, O, N, and C elements were supported by EDX analysis.

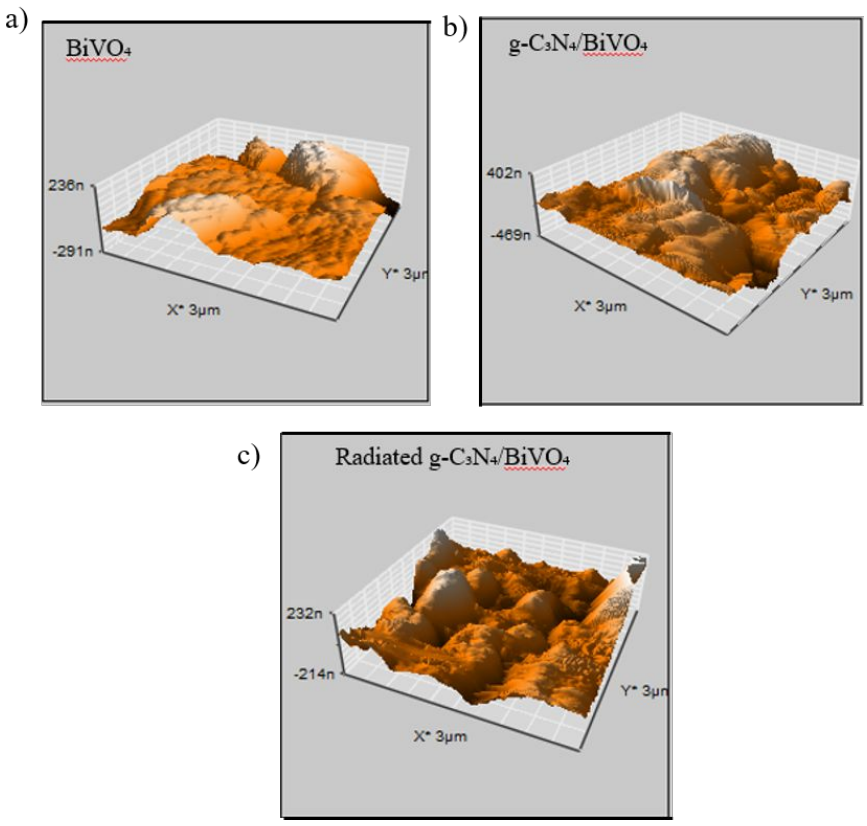

Fig. 9 Atomic force microscopy (AFM) images of $BiVO_4$ and gamma radiated g-C_3N_4@$BiVO_4$.

Table 2: Surface roughness and thickness of $BiVO_4$, g-C_3N_4@$BiVO_4$, and gamma radiated g-C_3N_4@$BiVO_4$.

Sample	$BiVO_4$	g-C_3N_4@$BiVO_4$	Radiated g-C_3N_4@$BiVO_4$
Surface roughness (nm)	36.478	43.191	57.984
Thickness (nm)	321.7	443.1	483.0

Fig. 10 shows a cross section of $BiVO_4$ and g-C_3N_4 treated with gamma radiation along with their corresponding $BiVO_4$. The morphology of $BiVO_4$ shows different thickness. For the $BiVO_4$, the average thickness is in the range of 305.2 ~ 335.0 nm. The thickness will increase to double in the range 405.4 ~ 584.6 nm when the heterojunction is established.

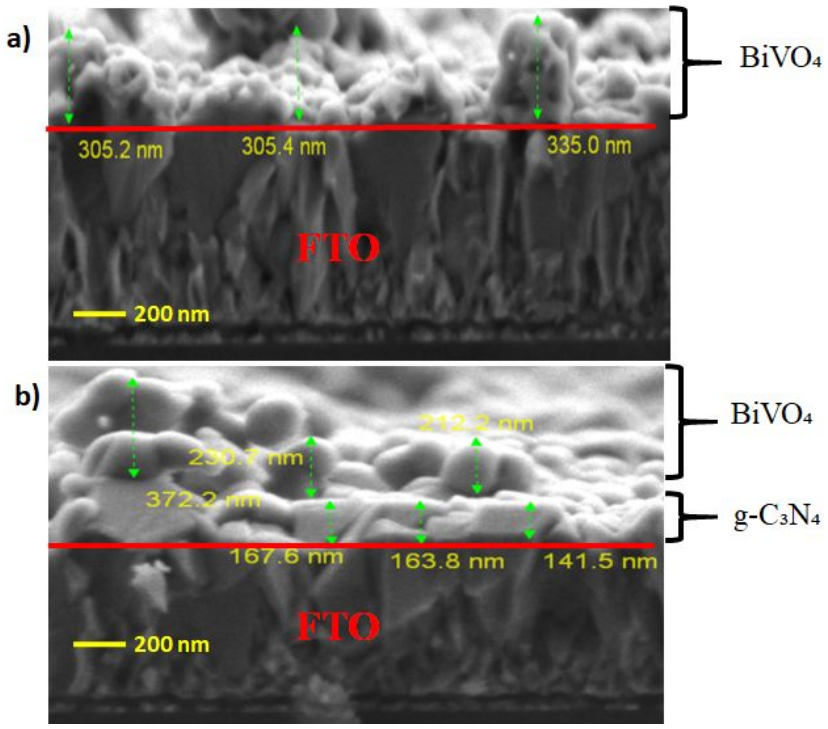

Fig. 10 FESEM cross sectional images of $BiVO_4$ and gamma radiated g-C_3N_4@$BiVO_4$

3.6 PEC performance

As discussed above, g-C_3N_4 is a great potential material for photocatalytic reaction and has received an intensive attention due to its unique electronic property such as visible light response, good reduction ability, easy synthesis and have a high stability. So, gamma radiation on g-C_3N_4 and its heterojunction with $BiVO_4$ have been used as useful approaches to enhances the PEC in water splitting. In this research, the effect of gamma

radiation on g-C_3N_4 at the dose of 2, 4, 6, 8, and 10 Gy was discussed and compared with the non-irradiated samples.

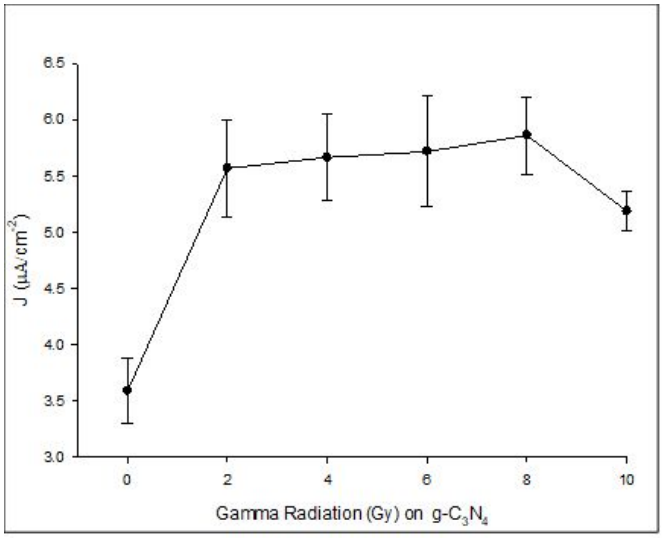

Fig. 11 J-V versus gamma radiation on g-C_3N_4. Error bars display one standard deviation from the mean of four replicate.

Comparative analysis the data from (Fig. 11) led us to conclude that the different doses resulted in the different performance of g-C_3N_4 semiconductor. Clearly, a lower dose of gamma radiation was found to increase the current density quite linearly from 2 Gy to 8 Gy, whereas the current density decreases at 10 Gy. Gamma radiation on solid material produces microstructural change which in turn changes the optical and other properties of the material [68]. Furthermore, there are two process occur when gamma radiation

interacts with the material, defect creation and defect annihilation. This can be seen in (Fig. 2) as the chemical structure of g-C_3N_4 was altered by gamma radiation which led to the improvement of the photocurrent density from 3.59 μAcm^{-2} g-C_3N_4, to 5.86 μAcm^{-2} for unirradiated and irradiated g-C_3N_4, respectively (Fig. 11). The changes properties of the material will depend on these two processes or on the other hand it depends on the irradiation dose. This is due to higher doses of gamma radiation, the number of defects created becomes more than the number of defects annihilated, the reverse is true at lower doses of gamma radiation. Gamma irradiation on materials may cause re-crystallization or amorphization depends on the nature of the material and irradiation dose of gamma radiation. From above discussion, the probability of recrystallization is more at lower doses of gamma radiation whereas the amorphization of the material is prominent at higher doses of gamma radiation.

However, g-C_3N_4 exhibit weak photocatalytic activity due to its wide bandgap energy (2.71 eV) [27,42,52] , which can be activated by visible light irradiation only. Herein, the idea of heterojunction with $BiVO_4$ as useful approach to improve the PEC water splitting. Fig. 12 shows a photocurrent density of gamma radiation of g-C_3N_4 heterojunction $BiVO_4$, and

non- irradiated g-C_3N_4 heterojunction with $BiVO_4$. For the $BiVO_4$, the current density is 0.34 mA/cm^2 at 1.23 V as reported by Seabold and Choi [31]. The current density increase linearly as shows in (Fig. 12), however it drops linearly at high dose such as 10 Gy of gamma radiation. The effects of ionizing radiation on metal oxide thin films depend on the radiation dose and parameters of the films, including the film thickness. Probably, due to the ionizing radiation from free radical with dose of 10 Gy, the physical properties such as optical and electrical alter the performance of the g-C_3N_4@$BiVO_4$ heterojunction.

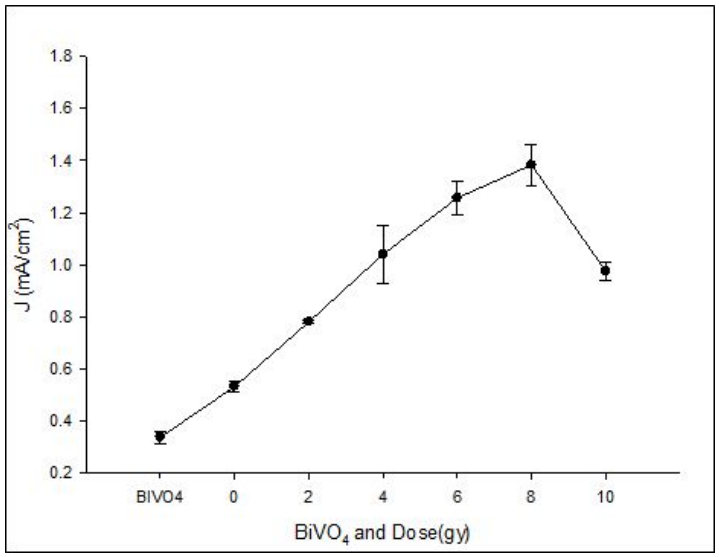

Fig. 12 Photocurrent density versus gamma radiation g-C_3N_4@$BiVO_4$. Error bars display one standard deviation from the mean of three replicate.

3.7 Photocurrent density versus voltage

In this study, the effect of gamma radiation on g-C_3N_4 semiconductor material (2, 4, 6, 8 and 10 Gy) was discussed and compared with the non-irradiated samples. The PEC performances were recorded by using 3 electrode configurations, such as g-C_3N_4 as working electrode, platinum as a counter electrode, and Ag/AgCl as references electrode; under 1.5 AM solar simulator with a 0.5 M Na_2SO_4 electrolyte. Photocurrent density versus potential (Voltage versus Ag/AgCl) shows a good photocatalytic response under both dark and visible light irradiations. In (Fig. 13a), a good photocatalytic response between g-C_3N_4 and gamma radiation g-C_3N_4 can be seen. Irradiated g-C_3N_4 has two-times better performance which increase from 3.59 to 5.86 μAcm^{-2} at 1.23V versus Ag/AgCl in 0.5 Na_2SO_4 electrolyte solution (pH 7). Ionizing radiation produces a free radical to induces chemical reaction, happen on semiconductor g-C_3N_4. The small difference between treated g-C_3N_4 and non-irradiated g-C_3N_4 shows that gamma radiation can change the electrical properties of the g-C_3N_4 and improve in PEC water splitting.

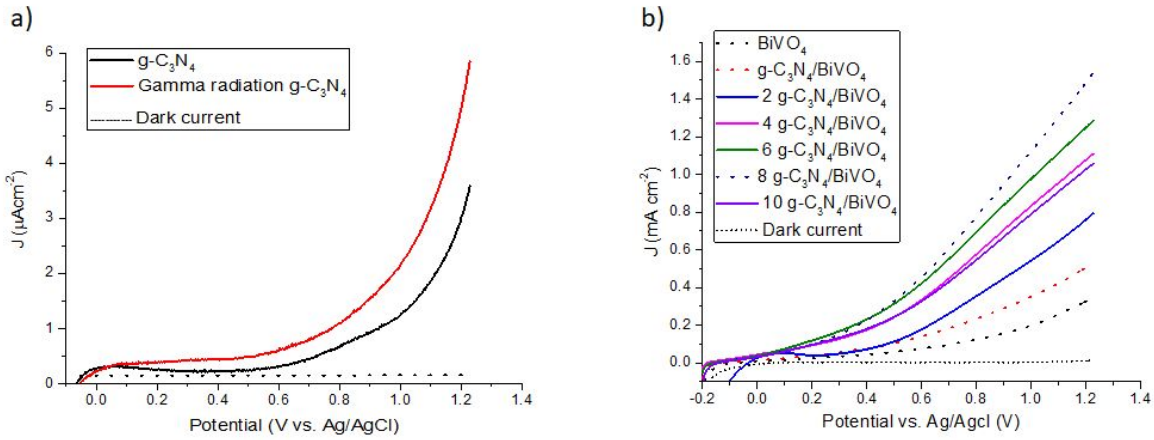

Fig.13 J-V curves for a) comparison of g-C_3N_4 and gamma radiated g-C_3N_4 (2, 4, 6, 8 and 10 Gy) b) J-V curve for $BiVO_4$, g-C_3N_4@$BiVO_4$ and gamma radiation g-C_3N_4@$BiVO_4$ in the dark and light illumination in 0.5 M Na_2SO_4 (pH7) electrolyte.

The photocurrent density versus potential (voltage versus Ag/AgCl) for $BiVO_4$ as a control, g-C_3N_4@$BiVO_4$ and gamma irradiated g-C_3N@$BiVO_4$ were investigated, which are shown in (Fig. 13b). $BiVO_4$ is an *n*-type semiconductor and serve as a photoanode which generate anodic photocurrent through the consumption of photoinduced holes for water oxidation at the semiconductor/electrolyte interface [25,27,31]. Under 100 $mWcm^{-2}$ light intensity, the photocurrent density recorded was 0.33 $mAcm^{-2}$ at 1.23 V versus Ag/AgCl.

Meanwhile, the photocurrent density increases almost two-times in case of g-C_3N_4@$BiVO_4$ heterojunction. In summary, studies have found that gamma radiation enhances the PEC water splitting performance of g-C_3N_4. Moreover, the photocurrent of gamma irradiated g-C_3N_4@$BiVO_4$ heterojunction increased from 0.78 to 1.38 $mAcm^{-2}$ by 2 Gy until 8 Gy. However, the photocurrent density decreased to 0.97 $mAcm^{-2}$ when 10 Gy of gamma radiation is used. Due to high dose of gamma radiation, ionizing radiation produces changes in the physical properties (such as optical, electrical and structural) of the material [8]. In this case, gamma radiation changes the chemical bonding as discussed in (Fig. 2-3). Under dark current situation, the photocurrent was almost negligible and showed high response after being illuminated. So, it can be concluded that light has been absorbed by FTO and results less photocurrent which consequences fewer pinholes in the photoanode and can ultimately reduce its photocurrent density.

Furthermore, photocurrent density of treated g-C_3N_4 and non-treated g-C_3N_4 with spin coating technique, responsive to the light and dark are shown in (Fig.14a). Analysis of this figure consequences that current occurs in light at - 0.1 V which indicates the

recombination process between the semiconductor and electrolyte. So, spin coating method is important to ensure the g-C_3N_4 was deposited uniformly on thin film to prevent the pinholes. High surface area of g-C_3N_4 results in higher light absorption which will further increase the current density.

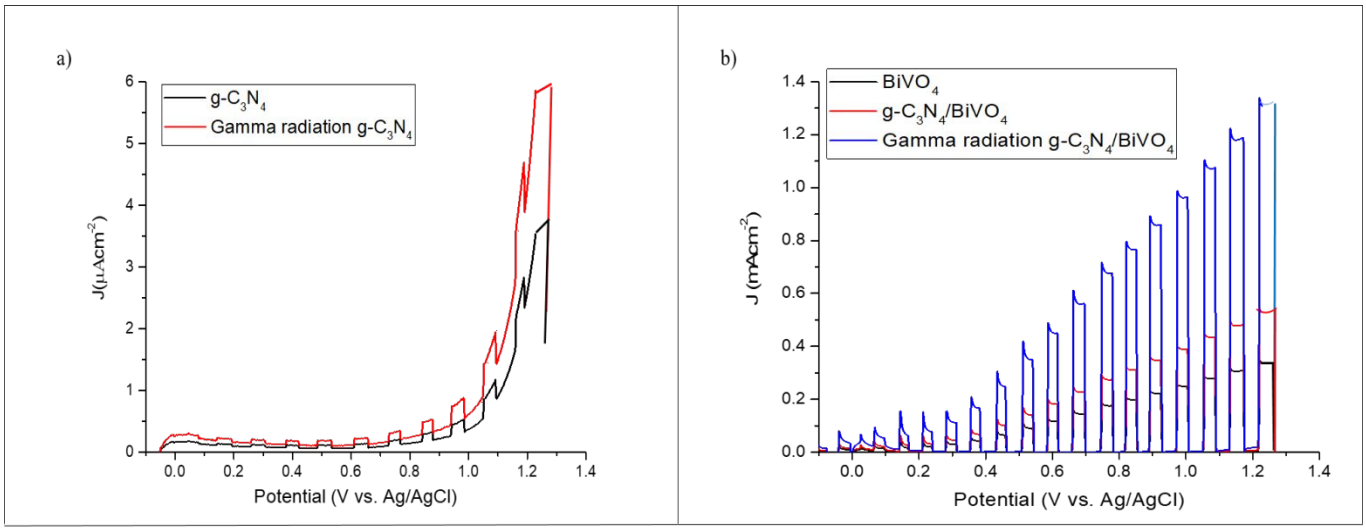

Fig. 14 a) Photoresponse of g-C_3N_4 and gamma treated g-C_3N_4 b) photoresponse of $BiVO_4$, g-C_3N_4@$BiVO_4$ and gamma irradiated (8Gy) on g-C_3N_4@$BiVO_4$ under light and dark in 0.5 M Na_2SO_4.

The photoresponse pattern of thin film $BiVO_4$, g-C_3N_4@$BiVO_4$ and gamma radiated g-C_3N_4@$BiVO_4$, under the light and dark at 100 Mw cm^{-2} light intensity is shown in (Fig. 14b) Comparative analysis of these pattern show that all material represents a

photoactive thin film. It is known that a short deposition time results thinner films, whereas a longer time corresponds to thicker films, therefore that is why 5 minutes of time deposition has been selected. As the films thickness increase, the sample produces lower photocurrent density. This might be due to the greater distance travelled by the charge carriers, thereby increasing the recombination rate of electron-hole pairs. In case of thinnest films, the short distance travelled by charge carriers compared to its diffusion length. Therefore, the charge carriers do not have enough time to diffuse to electron-hole pairs. Lastly, the as-fabricated heterojunction demonstrated a negligible photocurrent reduction under 395 nm cut-off filter, affirming the high contribution of visible light in photo-generation and transportation of exciton (Fig. S1).

3.8 Photocatalytic mechanisms

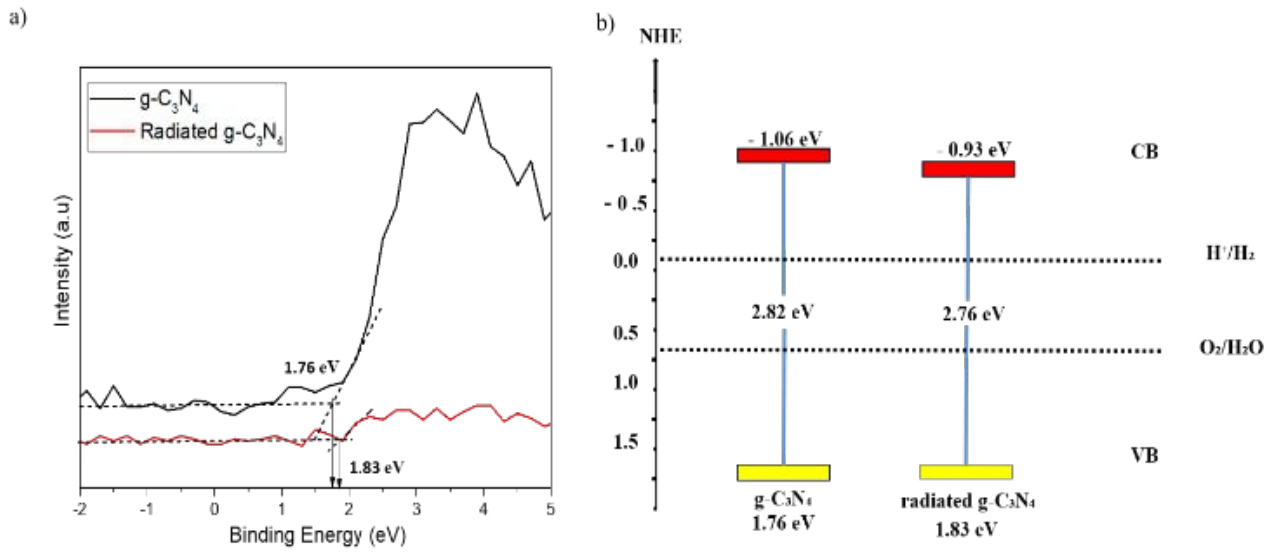

Fig. 15 a) Valence band XPS spectra of g-C_3N_4 and radiated g-C_3N_4.b) Schematic illustration of the band structures of -C_3N_4 and radiated g-C_3N_4.

The efficiency of separation and transfer of photoinduced electron-hole was known as the key factor to improve the photocatalytic activity [42,69].The potential positions of the conduction band (CB) and valence band (VB) of g-C_3N_4 may affect the efficiency of separation and transfer of photoinduced electron-hole. A comparison of radiated g-C_3N_4 and unirradiated g-C_3N_4 was examined by the valence band X-ray photoelectron spectroscopy (VB XPS). The values of E_{VB} for g-C_3N_4 and radiated g-C_3N_4 were revealed to be about 1.76 eV and 1.83 eV. Band gap which is referred to Eg, was estimated to be

about 2.82 eV and 2.76 eV from previously obtained Tauc-plots, respectively. Using the formula, $E_{CB}=E_{VB}-E_g$, the values of ECB was calculated to be about -1.06 eV and -0.93 eV. In short, (Fig.15b) shows that the conduction band and valence band potentials of g-C_3N_4 respectively became less negative and more positive upon gamma radiation. As it was demonstrated in (Fig. 3), both N1s and C1s orbitals underwent hybridization upon gamma irradiation. Since the VB of g-C_3N_4 is principally comprised of N1s orbitals while its CB mainly consists of C1s orbitals, both valence and conduction band energies of g-C_3N_4 are modified upon gamma radiation [27,52].

3.9 First Principles study of g-C_3N_4@$BiVO_4$ Heterojunction

The experimental data of g-C_3N_4@$BiVO_4$ Heterojunction is reproduced from DFT simulations. DFT simulations are carried out for individual $BiVO_4$(001), g-C_3N_4, and g-C_3N_4@$BiVO_4$(001) heterostructure, relaxed structures are shown in (Fig. 16). Our theoretical data predict that g-C_3N_4@$BiVO_4$ has negligible mismatch (0.02 %), which finally consequences its strong overapplying. Before making heterojunction, the surface stability of $BiVO_4$(001) is confirmed from its positive surface formation energy of 1.95 J/m^2. So, due to it stability, $BiVO_4$(001) slab was chosen to construct g-C_3N_4@$BiVO_4$(001)

heterostructure. The construction of g-C_3N_4@$BiVO_4$(001) heterostructure by placing a single layer of g-C_3N_4 on the top of $BiVO_4$(001) slab, see (Fig. 16c). Hereafter, the g-C_3N_4@$BiVO_4$(001) will be denoted as g-C_3N_4@$BiVO_4$.

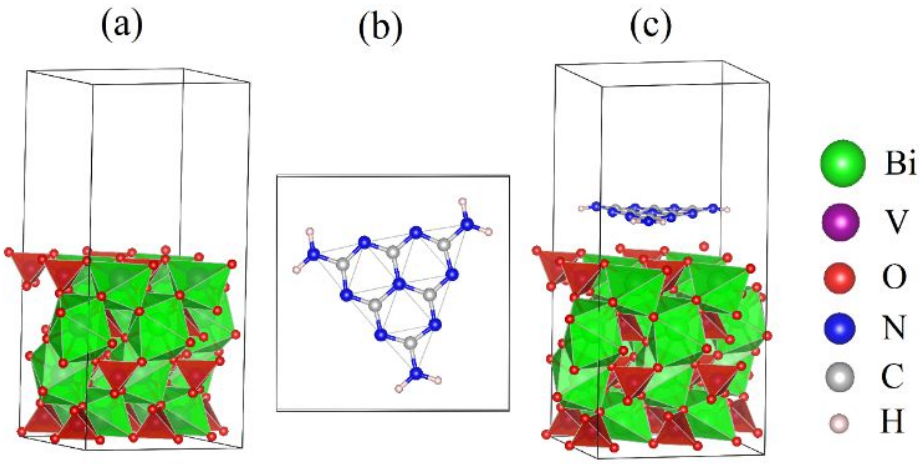

Fig. 16 Optimized crystal structures of (a) $BiVO_4$(001), (b) gC_3N_4 and (c) gC_3N_4@$BiVO_4$(001) heterojunction.[27]

From the relaxed crystal structure of heterojunction, it is found that g-C_3N_4 form a non-covalent bondings with the surface of $BiVO_4$ through Bi—N, O—C, and O—N; reveals strong van der Waal interaction between them. Moreover, the calculated adsorption energy of g-C_3N_4 nanosheet over the $BiVO_4$(001) is -0.68 eV which also confirm the

thermodynamic stability of g-C_3N_4@$BiVO_4$ heterojunction. The adsorption or interface adhesion formation energy was calculated with the help of eq 2.

$$\Delta E_{ad} = E_{g\text{-}C3N4@BiVO4} - (E_{g\text{-}C3N4} + E_{BiVO4(001)}) \quad (2)$$

where $E_{g\text{-}C3N4@BiVO4}$, $E_{g\text{-}C3N4}$, and $E_{BiVO4(001)}$ represent the total energy of the relaxed g-$_3N_4$/$BiVO_4$ heterojunction, monolayer g-C_3N_4, and $BiVO_4$(001) slab, respectively. The electronic properties of g-C_3N_4@$BiVO_4$ heterostructure such as band structure and PDOS are simulated, to double check the experimental data. The simulated band structure of g-C_3N_4@$BiVO_4$ is shown in (Fig. 17), where an indirect bandgap of 2.46 eV is consistent with our experimentally observed band gap.

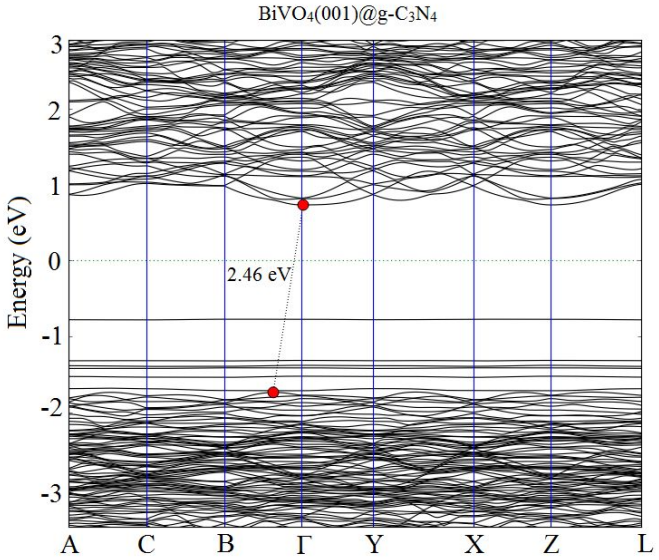

Fig. 17 Band structure of gC_3N_4@$BiVO_4$ heterojunction.[27]

The VBM of g-C_3N_4@$BiVO_4$ heterostructure is located between B and Γ points, whereas the CBM is at Γ point (see Fig. 17). Upon interaction of g-C_3N_4 with $BiVO_4$ (001), flat bands are produced in the VB of the resulted heterojunction, responsible for the VB of heterojunction which consequently lead to holes trapping. The enhanced overall photocatalytic activity or high charge carrier mobility can be related to these flat bands. The contribution of individual atoms in the resulted heterojunction, which make either VBM or CBM; the partial density of state (PDOS) are calculated which are shown in (Fig. 18).

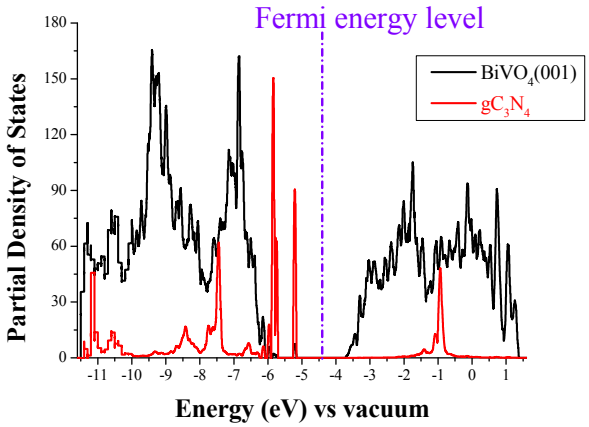

Fig. 18 PDOS plots of $BiVO_4$(001) and gC_3N_4 in gC_3N_4@$BiVO_4$ heterojunction.[27]

In case of g-C_3N_4@$BiVO_4$ heterojunction, the VB is occupied by the N and C orbitals of g-C_3N_4, while the CB is dominated by the 5d anti-bonding orbitals of V of $BiVO_4$. With respect to the vacuum level, both the VBM and CBM of g-C_3N_4@$BiVO_4$ heterojunction are situated at -6.16 and -3.70 eV, respectively, which has nice correlation with our experimental data. As can be seen from (Fig. 18), the VB and CB of heterojunction are at appropriate position while the Fermi energy result an internal electric field in the heterojunction; responsible for efficient photogenerated electrons and holes. The photogenerated electrons from CB of g-C_3N_4 directly reduce water and produce H_2 while holes at VB of $BiVO_4$ directly oxidize water and results O_2. On the other hand, electrons from CB of $BiVO_4$ recombine with the holes from the VB of g-C_3N_4. Finally, the internal built in van der Waal interactive forces (at the interface of g-C_3N_4@$BiVO_4$) will reduce the charge recombination.

The charge transfer between g-C_3N_4 and $BiVO_4$ in g-C_3N_4/$BiVO_4$ heterojunction was calculated from the charge density difference of the g-C_3N_4/$BiVO_4$ heterostructure, and the results are shown in (Fig. 19). The blue shaded areas represent charge accumulation

and depletion, respectively, so charge distribution occurred at the interface of g-C_3N_4@$BiVO_4$ heterostructure. The charge redistribution at g-C_3N_4@$BiVO_4$ heterostructure led us to predict that the electrons from the CB of g-C_3N_4 reduce water while the holes at the VB of $BiVO_4$ oxidize water to produce O_2. The quantity of this change of charge density is calculated from Bader charge analysis of the g-C_3N_4/$BiVO_4$ heterostructure which is about 0.056 electrons.

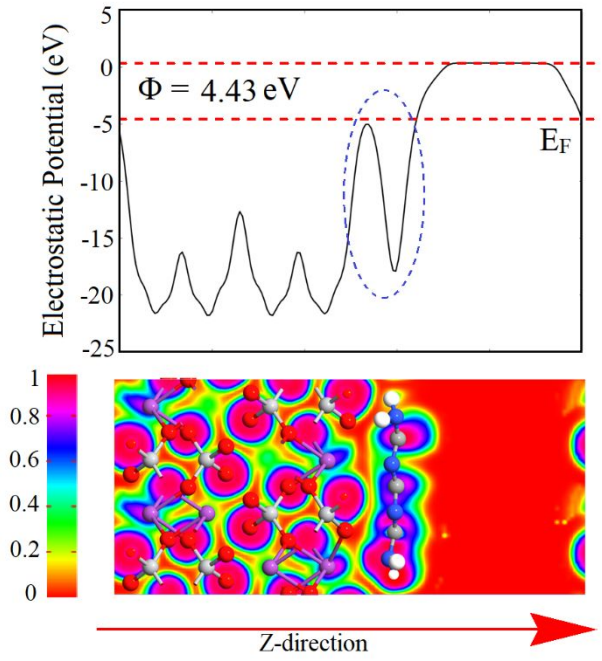

Fig. 19. Electrostatic potential map of gC_3N_4@$BiVO_4$ heterojunction along Z-direction.[27]

4. Conclusion

The effect of gamma radiation on the photoelectrochemical performance of and its heterojunction (g-C_3N_4@$BiVO_4$) have been carried out, characterized and confirmed by X-Ray diffraction (XRD), Fourier-transform infrared (FT-IR), X-ray photoelectron spectroscopy (XPS), Field Emission Scanning Electron Microscopy with Energy Dispersive X-Ray (FESEM-EDX), Ultraviolet and visible (UV-Vis), Atomic force microscope (AFM), Profilometer, Photocurrent Density (LSV), and Density Functional Theory (DFT) simulations. It is observed that the gamma radiation changes the structural and chemical structure of the semiconductor which ultimately improve the overall PEC efficiency. The band gap energy of gamma irradiated g-C_3N_4 reduces from 2.82 to 2.76 eV and the photocurrent density became two times to that of non-irradiated one; increased from 3.59 to 5.86 μA cm^{-2} at 1.23V vs. Ag/AgCl. Furthermore, the irradiated g-C_3N_4 was combined with $BiVO_4$ to form g-C_3N_4@$BiVO_4$ heterojunction, which has also two-timed photocurrent compared to that of non-radiated heterojunction; increased from 0.53 to 1.38 mA cm^{-2}. In summary, two different strategies have been applied (gamma radiation and heterojunction) on a single photoelectrode which has effectively increase the photoelectrochemical (PEC) efficiency of solar water splitting.

Supporting Information

Figure of the J-V curves for $BiVO_4$, g-C_3N_4@$BiVO_4$, and gamma radiated g-C_3N_4@$BiVO_4$.

The Supporting Information is available free of charge on the ACS Publications website.

Corresponding Author:

*E-mail: hu203@exeter.ac.uk (H.U); asri@ukm.edu.my (M.A.M.T)

Acknowledgements

The authours would like to acknowledge financial support from National University of Malaysia through internal grant GUP-2016-089 and GUP-2018-113, staff of UKM Centre for Research and Instrumentation (CRIM) and also Nuclear Sciences program for effort and support throughout this research. H.U. acknowledges Dr Andrew Cowley and the supercomputing facilities of Beowulf Cluster, University of Exeter, UK.

References

(1) Hu, S.; Xiang, C.; Haussener, S.; Berger, A. D.; N. S. Lewis. *Energy & Env. Sci*; **2013**, *6*, 2984–2993.

(2) Alfaifi, B. Y.; Ullah, H.; Alfaifi, S.; Tahir, A. A.; Mallick, T. K. Photoelectrochemical Solar Water Splitting: From Basic Principles to Advanced Devices. *Veruscript Funct. Nanomater.* **2018**.

(3) Walter, M. G.; Warren, E. L.; McKone, J. R.; Boettcher, S. W.; Mi, Q.; Santori, E. A.; Lewis, N. S. Solar Water Splitting Cells. *Chem. Rev. (Washington, DC, United States)* **2010**, *110*, 6446–6473.

(4) Rajeshwar, K. J. Hydrogen Generation at Irradiated Oxide Semiconductor-Solution Interfaces. *Electrochem* **2007**, *37*, 765–787.

(5) Fujishima, A.; Honda, K. Electrochemical Photolysis of Water at a Semiconductor Electrode. *Nature* **1972**, *37*, 238.

(6) Han, J.-M.; Wu, N.; Wang, B.; Wang, C.; Xu, M.; Yang, X.; Yang, H.; Zang, L. Gamma Radiation Induced Self-Assembly of Fluorescent Molecules into Nanofibers: A Stimuli-Responsive Sensing. *J. Mater. Chem. C* **2015**, *3*, 4345–4351.

(7) Knief, R. A. Radiation Effects and Damage. In *Nuclear Energy Technology*, McGraw-Hill, 1981; p 72.

(8) Mohil, M.; Kumar, G. A. Gamma Radiation Induced Effects in TeO_2 Thin Films. *J. Nano- Electron. Phys.* **2013**, *5*, 5–7.

(9) Ch, R.; Hail, A.; Hussein, H. F.; Al-fregi, A. A. The Effect of Gamma-Irradiation on the Absorption Spectra and Optical Energy Gap of Selenium Dioxide Thin Films. *Sci. J. Phys.* **2012**, 3–6.

(10) Egorova, E. M.; Revina, A. A. Optical Properties and Sizes of Silver Nanoparticles in Micellar Solutions. *Colloid J.* **2002**, *64*, 301–311.

(11) Gornostaeva, S. V.; Fenin, A. A.; Revina, A. A.; Ermakov, V. I. Influence of the Composition of the Inverse Micelle Solution on the Formation of Nickel Nanoparticles under the Effect of γ-Rays of 60Co. *Theor. Found. Chem. Eng.* **2008**, *42*, 599–602.

(12) Revina, A. A.; Oksentyuk, E. V.; Fenin, A. A. Synthesis and Properties of Zinc Nanoparticles: The Role and Prospects of Radiation Chemistry in the Development of Modern Nanotechnology. *Prot. Met.* **2007**, *43*, 554–559.

(13) Yonghong, N.; Xuewu, G.; Zhicheng, Z. γ-Irradiation Preparation of CdS Nano-

Particles and Their Formation Mechanism in Non-Water System. *Mater. Sci. Eng. B-Solid* **2006**, *130*, 61.

(14) Alarcon, J.; Ponce, S.; Paraguay-Delgado, F.; Rodriguez, J. Effect of Gamma-Irradiation on the Growth of ZnO Nanorod Films for Photocatalytic Disinfection of Contaminated Water. *J. Colloid Interface Sci.* **2011**, *364*, 49–55.

(15) Al-Hamdani, N. A.; Al-Alawy, R. D.; Hassan, S. J. Effect of Gamma Irradiation on the Structural and Optical Properties of ZnO Thin Films. *IOSR J. Comput. Eng.* **2014**, *16*, 11–16.

(16) Yu, J.; Wang, S.; Cheng, B.; Lin, Z.; Huang, F. Noble Metal-Free Ni(OH)2–g-C3N4 Composite Photocatalyst with Enhanced Visible-Light Photocatalytic H2-Production Activity. *Catal. Sci. Technol.* **2013**, *3*, 1782.

(17) Zhang, G.; Zang, S.; Wang, X. Layered Co(OH)2 Deposited Polymeric Carbon Nitrides for Photocatalytic Water Oxidation. *ACS Catal.* **2015**, *5*, 941–947.

(18) Lu, M.; Pei, Z.; Weng, S.; Feng, W.; Fang, Z.; Zheng, Z.; Huang, M.; Liu, P. Constructing Atomic Layer G-C_3N_4–CdS Nanoheterojunctions with Efficiently

Enhanced Visible Light Photocatalytic Activity. *Phys. Chem. Chem. Phys.* **2014**, *16*, 21280–21288.

(19) Hong, J.; Wang, Y.; Wang, Y.; Zhang, W.; Xu, R. Noble-Metal-Free NiS/C3N4 for Efficient Photocatalytic Hydrogen Evolution from Water. *ChemSusChem* **2013**, *6*, 2263–2268.

(20) Wu, Z.; Gao, H.; Yan, S.; Zou, Z.; Zhao, J.; Ma, L.; Wang, H.; Zhao, Y.; Zhang, J.; Hu, S.; et al. Microwave-Assisted Molten-Salt Rapid Synthesis of Isotype Triazine-/Heptazine Based g-C3N4 heterojunctions with Highly Enhanced Photocatalytic Hydrogen Evolution Performance. *Appl. Catal. B Environ.* **2017**, *81*, 21497–21509.

(21) Wang, J.; Guo, P.; Guo, Q.; Jonsson, P. G.; Zhao, Z. Fabrication of Novel g-C3N4/Nanocage ZnS Composites with Enhanced Photocatalytic Activities under Visible Light Irradiation. *CrystEngComm* **2014**, *16*, 4485–4492.

(22) Jiang, D.; Chen, L.; Xie, J.; Chen, M. Ag_2 S/g-C_3N_4 Composite Photocatalysts for Efficient Pt-Free Hydrogen Production. The Co-Catalyst Function of Ag/Ag_2S Formed by Simultaneous Photodeposition. *Dalt. Trans.* **2014**, *43*, 4878–4885.

(23) Fang, H. Bin; Luo, Y.; Zheng, Y. Z.; Ma, W.; Tao, X. Facile Large-Scale Synthesis of Urea-Derived Porous Graphitic Carbon Nitride with Extraordinary Visible-Light Spectrum Photodegradation. *Ind. Eng. Chem. Res.* **2016**, *55*, 4506–4514.

(24) Dong, F.; Zhao, Z.; Xiong, T.; Ni, Z.; Zhang, W.; Sun, Y.; Ho, W.-K. In Situ Construction of G-C3N4/g-C N 4 Metal-Free Heterojunction for Enhanced Visible-Light Photocatalysis. *ACS Appl. Mater. Interfaces* **2013**, *5*, 11392–11401.

(25) Nasir, S. N. F. M.; Ullah, H.; Ebadi, M.; Tahir, A. A.; Sagu, J. S.; Mat Teridi, M. A. New Insights into Se/$BiVO_4$ Heterostructure for Photoelectrochemical Water Splitting: A Combined Experimental and DFT Study. *J. Phys. Chem. C* **2017**, *121*, 6218–6228.

(26) Mohd-Nasir, S. N. F.; Mat-Teridi, M. A.; Ebadi, M.; Sagu, J. S.; Sulaiman, M. Y.; Ludin, N. A.; Ibrahim, M. A. Influence of Ethylene Glycol on Efficient Photoelectrochemical Activity of BiVO4 Photoanode via AACVD. *Phys. Status Solidi Appl. Mater. Sci.* **2015**, *212*, 2910–2914.

(27) Safaei, J.; Ullah, H.; Mohamed, N. A.; Mohamad Noh, M. F.; Soh, M. F.; Tahir, A.

A.; Ahmad Ludin, N.; Ibrahim, M. A.; Wan Isahak, W. N. R.; Mat Teridi, M. A. Enhanced Photoelectrochemical Performance of Z-Scheme g-C_3N_4/$BiVO_4$ Photocatalyst. *Appl. Catal. B Environ.* **2018**, *234*.

(28) Hanna, M. C.; Nozik, A. J. Solar Conversion Efficiency of Photovoltaic and Photoelectrolysis Cells with Carrier Multiplication Absorbers. *J. Appl. Phys.* **2006**, *100* (7).

(29) Xie, B.; Zhang, H.; Cai, P.; Qiu, R.; Xiong, Y. Simultaneous Photocatalytic Reduction of Cr(VI) and Oxidation of Phenol over Monoclinic $BiVO_4$ under Visible Light Irradiation. *Chemosphere* **2006**, *63*, 956–963.

(30) Yan, S. C.; Li, Z. S.; Zou, Z. G. Photodegradation of Rhodamine B and Methyl Orange over Boron-Doped g-C_3N_4 under Visible Light Irradiation. *Langmuir* **2010**, *26*, 3894–3901.

(31) Seabold, J. A.; Choi, K. S. Efficient and Stable Photo-Oxidation of Water by a Bismuth Vanadate Photoanode Coupled with an Iron Oxyhydroxide Oxygen Evolution Catalyst. *J. Am. Chem. Soc.* **2012**, *134*, 2186–2192.

(32) AtomistixTool. Version 2017.1, QuantumATK A/S (www.Quantumwise.Com).

(33) VirtualNanoLab. Version 2017.1, Quantumwise A/S. (www.Quantumwise.Com).

(34) Sleight, A. W.; Chen, H.-Y.; Ferretti, A. Crystal Growth and Structure of $BiVO_4$. *Mater. Res. Bull.* **1979**, *14*, 1571–1581.

(35) Xi, G.; Ye, J. Synthesis of Bismuth Vanadate Nanoplates with Exposed {001} Facets and Enhanced Visible-Light Photocatalytic Properties. *Chem. Commun.* **2010**, *46*, 1893–1895.

(36) Enkovaara, J.; Rostgaard, C.; Moetensen, J. .; Chen, J.; Dulak, M.; Ferrighi, L.; Gavnholt, J.; Glinsvad, C.; Haikola, V.; Hansen, H. Electronic Structure Calculations with GPAW: A Real-Space Implementation of the Projector Augmented-Wave Method. *J.Phys Condens. Matter* **2010**, *22*, 253202.

(37) Kresse, G.; Joubert, D. From Ultrasoft Pseudopotentials to the Projector Augmented-Wave Method. *Phys. Rev. B* **1978**, *59*, 1999.

(38) Tran, F.; Blaha, P. Accurate Band Gaps of Semiconductors and Insulators with a

Semilocal Exchange-Correlation Potential. *Phys. Rev. Lett.* **2009**, *102*, 5–8.

(39) Endres, J.; Egger, D. A.; Kulbak, M.; Kerner, R. A.; Zhao, L.; Silver, S. H.; Hodes, G.; Rand, B. P.; Cahen, D.; Kronik, L.; et al. Valence and Conduction Band Densities of States of Metal Halide Perovskites: A Combined Experimental-Theoretical Study. *J. Phys. Chem. Lett.* **2016**, *7*, 2722–2729.

(40) Li, Q.; He, Y.; Peng, R. Graphitic Carbon Nitride (g-C_3N_4) as a Metal-Free Catalyst for Thermal Decomposition of Ammonium Perchlorate. *RSC Adv.* **2015**, *5*, 24507–24512.

(41) Maeda, K.; Wang, X.; Nishihara, Y.; Lu, D.; Antonietti, M.; Domen, K. Photocatalytic Activities of Graphitic Carbon Nitride Powder for Water Reduction and Oxidation under Visible Light. *J. Phys. Chem. C* **2009**, *113*, 4940–4947.

(42) Safaei, J.; Mohamed, N. A.; Mohamad Noh, M. F.; Soh, M. F.; Riza, M. A.; Mustakim, N. S. M.; Ludin, N. A.; Ibrahim, M. A.; Wan Isahak, W. N. R.; Mat Teridi, M. A. Facile Fabrication of Graphitic Carbon Nitride ,(g-C_3N_4) Thin Film. *J. Alloys Compd.* **2018**, *769*, 130–135.

(43) Tokunaga, S.; Kato, H.; Kudo, A. Selective Preparation of Monoclinic and Tetragonal $BiVO_4$ with Scheelite Structure and Their Photocatalytic Properties. *Chem. Mater.* **2001**, *13*, 4624–4628.

(44) Mohamad Noh, M. F.; Soh, M. F.; Riza, M. A.; Safaei, J.; Mohd Nasir, S. N. F.; Mohamad Sapian, N. W.; Teh, C. H.; Ibrahim, M. A.; Ludin, N. A.; Mat Teridi, M. A. Effect of Film Thickness on Photoelectrochemical Performance of SnO_2 Prepared via AACVD. *Phys. Status Solidi* **2018**, *1700570*, 1700570.

(45) Safaei, J.; Mohamed, N. A.; Mohamad Noh, M. F.; Soh, M. F.; Elbreki, A. M.; Ludin, N. A.; Ibrahim, M. A.; Al-Waeli, A. H. A.; Wan Isahak, W. N. R.; Mat Teridi, M. A. Simultaneous Enhancement in Light Absorption and Charge Transportation of Bismuth Vanadate ($BiVO_4$) Photoanode via Microwave Annealing. *Mater. Lett.* **2018**, *233*, 67–70.

(46) Meng, J.; Pei, J.; He, Z.; Wu, S.; Lin, Q.; Wei, X.; Li, J.; Zhang, Z. Facile Synthesis of g-C_3N_4 Nanosheets Loaded with WO_3 Nanoparticles with Enhanced Photocatalytic Performance under Visible Light Irradiation. *RSC Adv.* **2017**, *7*,

24097–24104.

(47) Jin, A.; Jia, Y.; Chen, C.; Liu, X.; Jiang, J.; Chen, X.; Zhang, F. Efficient Photocatalytic Hydrogen Evolution on Band Structure Tuned Polytriazine/Heptazine Based Carbon Nitride Heterojunctions with Ordered Needle-like Morphology Achieved by an in Situ Molten Salt Method. *J. Phys. Chem. C* **2017**, *121*, 21497–21509.

(48) Dong, F.; Wang, Z.; Sun, Y.; Ho, W. K.; Zhang, H. Engineering the Nanoarchitecture and Texture of Polymeric Carbon Nitride Semiconductor for Enhanced Visible Light Photocatalytic Activity. *J. Colloid Interface Sci.* **2013**, *401*, 70–79.

(49) Zhang, Y.; Guo, Y.; Duan, H.; Li, H.; Sun, C.; Liu, H. Facile Synthesis of V 4+ Self-Doped, [010] Oriented $BiVO_4$ Nanorods with Highly Efficient Visible Light-Induced Photocatalytic Activity. *Phys. Chem. Chem. Phys.* **2014**, *16*, 24519–24526.

(50) Knoll, G, F. Radiation Detection and Mesurement 4th Ed; 2010, 47–51.

(51) Peng, D.; Wang, H.; Yu, K.; Chang, Y.; Ma, X.; Dong, S. Photochemical Preparation

of the Ternary Composite CdS/Au/g-C_3N_4 with Enhanced Visible Light Photocatalytic Performance and its Microstructure. *RSC Adv.* **2016**, *6*, 77760–77767.

(52) Safaei, J.; Mohamed, N. A.; Noh, M. F. M.; Soh, M. F.; Ludin, N. A.; Mohd Adib Ibrahim; Wan Isahak, W. N. R.; Teridi, M. A. M. Graphitic Carbon Nitride (g-C_3N_4) Electrodes for Energy Conversion and Storage: A Review on Photoelectrochemical Water Splitting, Solar Cells and Supercapacitors. *J. Mater. Chem. A,* **2018**, *6*, 22346–22380.

(53) Ong, W.-J.; Tan, L.-L.; Chai, S.-P.; Yong, S.-T. Heterojunction Engineering of Graphitic Carbon Nitride (g-C_3N_4) via Pt Loading with Improved Daylight-Induced Photocatalytic Reduction of Carbon Dioxide to Methane. *Dalt. Trans.* **2015**, *44*, 1249.

(54) James, E. T. *Atoms, Radiation, and Radiation Protection*, 1st edition.; WILEY-VCH, 2007.

(55) Wei, B.; Vajtai, R.; Ajayan, P. Reliability and Current Carrying Capacity of Carbon

Nanotubes. *Appl. Phys. Lett.* **2001**, *79*, 1172–1174.

(56) Shiraishi, Y.; Kanazawa, S.; Sugano, Y.; Tsukamoto, D.; Sakamoto, H.; Ichikawa, S.; Hirai, T. Highly Selective Production of Hydrogen Peroxide on Graphitic Carbon Nitride (g-C_3N_4) Photocatalyst Activated by Visible Light. *ACS Catal.* **2014**, *4*, 774–780.

(57) Hong, J.; Xia, X.; Wang, Y.; Xu, R. Mesoporous Carbon Nitride with in Situ Sulfur Doping for Enhanced Photocatalytic Hydrogen Evolution from Water under Visible Light. *J. Mater. Chem.* **2012**, *22*, 15006.

(58) Ong, W. J.; Tan, L. L.; Ng, Y. H.; Yong, S. T.; Chai, S. P. Graphitic Carbon Nitride (g-C_3N_4)-Based Photocatalysts for Artificial Photosynthesis and Environmental Remediation: Are We a Step Closer to Achieving Sustainability? *Chem. Rev.* **2016**, *116*, 7159–7329.

(59) Su, Y.; Chen, P.; Wang, F.; Zhang, Q.; Chen, T.; Wang, Y.; Yao, K.; Lv, W.; Liu, G. Decoration of TiO_2/g-C_3N_4 Z-Scheme by Carbon Dots as a Novel Photocatalyst with Improved Visible-Light Photocatalytic Performance for the Degradation of

Enrofloxacin. *RSC Adv.* **2017**, *7*, 34096–34103.

(60) Arshak, K.; Kerostynska, O. Gamma Radiation Induced Changes in the Electrical and Optical Properties of Tellurium Dioxide Thin Films. *IEEE Sens. J.* **2003**, *3*, 717.

(61) Ahmad, S.; Khan, M. S.; Asokan, K.; Zulfequar, M. Effect of Gamma Irradiation on Structural and Optical Properties of Thin Films of A-Cd_5Se_{95}-XZn_x. *Int. J. Thin. Fil. Sci. Tec.* **2015**, *4*, 103–109.

(62) Alwan, T. J. Gamma Irradiation Effect on the Optical Properties and Refractive Index Dispersion of Dye Doped Polystyrene Films. *Turkish J. Phys.* **2012**, *36*, 377–384.

(63) Maity, T. K.; Sharma, S. L. Effects of Gamma Irradiation on Electrical, Optical and Structural Properties of Tellurium Dioxide Thin Films. *Indian J. Pure Appl. Phys.* **2011**, *49*, 606–612.

(64) Sahu, N.; Parija, B.; Panigrahi, S. Fundamental Understanding and Modeling of Spin Coating Process: A Review. *Indian J. Phys.* **2009**, *83*, 493–502.

(65) Mohd Nasir, S. N. F.; Yahya, M. K. N.; Mohamad Sapian, N. W.; Ahmad Ludin, N.; Ibrahim, M. A.; Sopian, K.; Mat Teridi, M. A. Heterojunction Cr_2O_3/CuO:Ni Photocathodes for Enhanced Photoelectrochemical Performance. *RSC Adv.* **2016**, *6*, 56885–56891.

(66) Noh, M. F. M.; Arzaee, N. A.; Safaei, J.; Mohamed, N. A.; Kim, H. P.; Yusoff, A. R. M.; Jang, J.; Teridi, M. Eliminating Oxygen Vacancies in SnO_2 Films via Aerosol-Assisted Chemical Vapour Deposition for Perovskite Solar Cells and Photoelectrochemical Cells. *J. Alloys Compd.* **2018**, *773*, 997–1008.

(67) Tahir, A. A.; Mat-Teridi, M. A.; Wijayantha, K. G. U. Photoelectrochemical Properties of Texture-Controlled Nanostructured α-Fe_2O_3 Thin Films Prepared by AACVD. *Phys. Status Solidi RRL,* **2014**, *981*, 976–981.

(68) Padiyan, D. P.; Marikani, A.; Murali, K. R. Influence of Thickness and Substrate Temperature on Electrical and Photoelectrical Properties of Vacuum-Deposited CdSe Thin Films. *Mater. Chem. Phys.* **2003**, *78*, 51–58.

(69) Mo, Z.; She, X.; Li, Y.; Liu, L.; Huang, L.; Chen, Z.; Zhang, Q.; Xu, H.; Li, H.

Synthesis of g-C_3N_4 at Different Temperatures for Superior Visible/UV Photocatalytic Performance and Photoelectrochemical Sensing of MB Solution. *RSC Adv.* **2015**, *5*, 101552–101562.

Table of Content